Semi-Annual Report Submitted to the
National Aeronautics and Space Administration

For July - December, 2000

Contract Number: NAS5-31370

Land Surface Temperature Measurements from EOS MODIS Data

ZHENGMING WAN

XIALIN MA

P.I.'s Address:

Zhengming Wan
Institute for Computational Earth System Science
University of California
Santa Barbara, CA 93106-3060

phone : (805) 893-4541
Fax no: (805) 893-2578
E-mail: wan@icess.ucsb.edu

Land Surface Temperature Measurements from EOS MODIS Data

Semi-Annual Report for July - December, 2000

Zhengming Wan and Xialin Ma

Abstract

Estimate of systematic error and noise in thermal infrared data of the Moderate Resolution Imaging Spectroradiometer (MODIS) was made with early MODIS data in 14 cases of sub-area sites with a size of 10 lines by 16 pixels each line, where the brightness temperature in band 31 changes within ± 0.1K. It is found that the ninth channel in bands 21 and 24, and the fourth channel in band 22 are too noisy to use. There are significant channel-dependent systematic errors in 1-3 channels in bands 22, 23, 25, 27-30. After correcting the channel-dependent systematic errors, the quality of the MODIS TIR data is significantly improved in bands 22-25, and 27-30, and the specification of noise equivalent temperature difference (NEDT) is reached in all but the three noisy channels of the 16 MODIS TIR bands. Results are given in the first paper submitted to Remote Sensing of Environment.

The estimate of calibration accuracy of MODIS TIR bands reported in the semi-annual report for January - June, 2000, has been updated with more comparison results between the band brightness temperatures from the reprocessed MODIS calibrated radiance product (version 2.5.4 of MOD021KM) and the calculated values based on in-situ measurements of lake surface temperature and atmospheric temperature/water vapor profiles. It is found that the calibration accuracy in bands 29, 31 and 32 is better than 0.5%, the specified absolute radiometric accuracy of 1% is reached or nearly reached in MODIS bands 21, 29 and 33-34, and also in band 30 if the true atmospheric column ozone is 6-12% below the value retrieved from the TOMS data. Comparisons indicate a calibration bias 2-3% in bands 20, 22 and 23. It is difficult to obtain a definitive estimate in bands 24-25, 27-28, and 35-36 because of the larger effects of the variations and uncertainties in atmospheric temperature and water vapor profiles. Results are given in the second paper submitted to Remote Sensing of Environment.

Significant progress has been made in simultaneous retrieval of land-surface temperature/emissivity and atmospheric profiles with MODIS data.

Recently Papers Submitted

Z. Wan, "Estimate of noise and systematic error in early thermal infrared data of the Moderate Resolution Imaging Spectroradiometer (MODIS)", Remote Sens. Environ., submitted November 2000.

Z. Wan, Y. Zhang, Z.-L. Li, R. Wang, V.V. Salomonson, A. Yves, and R. Bosseno, "Preliminary estimate of calibration of the Moderate Resolution Imaging Spectroradiometer (MODIS) thermal infrared data using Lake Titicaca", Remote Sens. Environ., submitted February 2001.

Introduction

In order to deal with the close coupling between land-surface and atmosphere, Dr. Paul Menzel and I decided that our two groups should work together to improve the qualities of MODIS atmospheric temperature/humidity profile and LST products. He sent Mr. Xia-lin Ma to UCSB in October 1997. Since then support for Mr. Ma has been shared by both our MODIS contracts. We worked together to extend the day/night LST algorithm into a new generalized day/night algorithm to simultaneously retrieve land-surface temperature/emissivity and atmospheric profiles with MODIS data. We have made significant progress in this new direction. The new algorithm has been tested with MAS and MODIS data, showing its ability to improve the accuracies of both the LST and atmospheric profile products. Detailed results are shown in the manuscript after this brief introduction.

Simultaneous retrieval of atmospheric profiles and land-surface temperature/emissivity from Moderate Resolution Imaging Spectroradiometer thermal infrared data: extension of a two-step physical algorithm

Xia L. Ma[1,2], Zhengming Wan[1], Christopher C. Moeller[2], W. Paul Menzel[3], and Liam E. Gumley[2]

[1] Institute for Computational Earth System Science, University of California, Santa Barbara, California, 93106

[2] Cooperative Institute for Meteorological Satellite Studies, University of Wisconsin-Madison, Madison, Wisconsin, 53706

[3] NOAA/NESDIS, Office of Research and Applications Advanced Satellite Products Team

Abstract

An extension to the two-step physical retrieval algorithm was developed. Combined clear-sky multitemporal and multispectral observations were used to retrieve atmospheric temperature-humidity profile, land-surface temperature and surface emissivities in the midwave (3-5 μm) and longwave (8-14.5 μm) regions. The extended algorithm was tested with both simulated and real Moderate Resolution Imaging Spectrodiometer (MODIS) Airborne Simulator (MAS) data. Sensitivity study and error analysis demonstrate that the retrieval performance is improved by the extended algorithm. The extended algorithm is relatively insensitive to the uncertainties simulated for the real observations. The extended algorithm was also applied to real MODIS daytime and nighttime observations illustrating that it is capable of retrieving medium-scale atmospheric temperature/water vapor profile and surface temperature/emissivity with similar retrieval accuracies as the Geostationary Operational Environmental Satellite (GOES) achieves plus much higher spatial resolution. Finally, possible further improvements are discussed, and a conclusion is drawn in the last section.

1. Introduction

An important objective in satellite remote sensing is the determination of accurate atmospheric temperature-humidity profile and land-surface or sea-surface temperature (hereafter referred to as LST and SST respectively) over the global domain. To help achieve this objective, the Earth Observing System (EOS) suite of instruments will provide global radiometric measurements for retrieving atmosphere, land and ocean properties from space. The specified accuracy for EOS atmospheric temperature is 1K root mean square error (rms) in 1km thick layer, 10% rms for tropospheric humidity, 0.3K for SST, and 1K for LST.

During the past two decades, there has been much research on retrieval of atmospheric temperature and moisture distribution as well as LST and SST. In physics-based retrievals it is important to consider all surface-atmospheric interactions and energy fluxes between the atmosphere and the surface since radiance measurements by airborne or satellite-borne multi-spectral infrared radiometers combine contributions from atmospheric absorption/emission and from surface emission and reflection. A variety of split-window methods have been developed to determine SST and LST using data from National Oceanic and Atmospheric Administration's (NOAA) Advanced Very High Resolution Radiometer (AVHRR). The split-window technique uses two spectral bands of different opacity within the 800-1000 cm^{-1} window region to correct atmospheric effects. McMillin[1-4] and others developed SST retrieval algorithms for NOAA multichannel SST (MCSST), cross-product SST (CPSST) and operational nonlinear SST (NLSST). Empirical coefficients are derived from regression analyses of AVHRR band brightness temperatures and in situ buoy measurements. The global standard errors of these algorithms are in the range

of 0.5-0.7K. More recently a new physics-based SST retrieval method was developed[5]. The algorithm requires a-priori specification of sea surface emissivity (reflectivity) spectra and atmospheric transmittance calculation. Error analyses have demonstrated that SST can theoretically be retrieved to within 0.22K rms using the High-resolution Interferometer Sounder (HIS) data or 0.51K using broadband split-window data provided that the a priori surface emissivity spectrum has a bias less than 0.5%. As for LST retrieval, simple extension to LST using the algorithm originally developed for SST would lead to unacceptable errors. Wan and Dozier[6] analyzed the major difficulties in the simple extension to the land surface of the split-window technique. Importantly, spectral variation of emissivity is much larger for different land-surface materials than water. For instance, large variations exist between vegetated and non-vegetated surfaces (e. g. rock, sand). Land-surface emissivity measurements show that surface emissivity varies from 0.85-0.99 in the split-window region, while sea-surface emissivity variation is much smaller (although sea-surface emissivity varies greatly with sea state). In addition, larger LST spatial variation and “mixed-pixel” fields of view (FOV) complicate the LST retrieval.

Significant effort has been made to estimate LST, including applying a variety of split-window methods[7-10]. Wan and Dozier[11] point out that the split-window algorithm requires surface emissivity knowledge to better than 0.01 to retrieve LST to accuracy of 1K. This is a difficult requirement to meet for land covers with variable emissivities, especially in semi-arid and arid areas. Li et. al.[13-14] proposed a scheme to retrieve surface spectral emissivity and LST using pairs of day/night co-registered AVHRR data. In their method, a temperature independent spectral index (TISI) in the thermal infrared bands is derived assuming that the surface thermal infrared bidirectional reflectance distribution function (BRDF) and atmospheric profile are known. Such a-priori information is rarely available. To relieve the a-

priori information requirement, a physics-based LST retrieval algorithm has been developed. The algorithm simultaneously retrieves daytime and nighttime LST, surface air temperature and total precipitable water-vapor (TWP), and surface spectral emissivity using MODIS day/night observations[15] under an assumption that surface emissivity is unchanged from daytime to nighttime. However, the physics-based LST retrieval is sensitive to the shape of the temperature and water vapor profile in the lower troposphere. Unfortunately, the shape of the lower atmospheric profile is poorly resolved by the spectral resolution of MODIS sensor. Thus the accuracy of the physics-based LST retrieval depends largely upon accurate atmospheric information.

Alternatively, remote sensing of atmospheric temperature-humidity profile from infrared emission bands usually requires assumptions about the emissivity of terrestrial materials. It is usually assumed that the earth's surface is a blackbody (emissivity 1.0)[16-21] or a gray-body (approximately 0.96-0.98)[22] for atmospheric sounding. These assumptions typically result in large retrieval errors over non-vegetated surfaces where surface emissivity spectral/spatial variations are prominent. Plokhenko and Menzel[23] point out that the surface emissivity must be considered in the physical retrieval solution because even small emissivity variations cause measurable changes in infrared radiance. Therefore, a two-step physical algorithm[24] (hereafter referred to as the "original" algorithm) was developed to include surface emissivity as a part of the solution of the radiative transfer equation (RTE). The original algorithm retrieves atmospheric temperature-humidity profile, surface temperature and surface emissivity in the midwave (3-5μm) and longwave (8-14.5μm) regions simultaneously from MODIS thermal infrared data. The algorithm was tested using both simulated and real MODIS Airborne Simulator (MAS) data. The original algorithm demonstrated that the accuracy of retrieved atmospheric and surface parameters is improved by including surface emissivity in the RTE. However, only two surface emissivities in the

window regions were retrieved, which may not adequately describe surface emissivity spectral variation, especially in the midwave region when non-vegetated surfaces are viewed. In addition, the improvement of retrieval accuracy of surface emissivities is rather limited. Unlike the Atmospheric Infrared Sounder (AIRS) or HIS with over 2000 spectral bands, the MODIS scanning ($\pm$55 degrees) spectroradiometer is limited to 36 bands (20 in the visible and near infrared range, and 16 in the 3-14.5μm region). Spectral characteristics of MODIS TIR bands and its prelaunch prototype MAS are listed in Tables 1 and 2. To obtain more information needed in retrieval, the surface-reflected solar beam in the midwave region might be a good external source since the emitted and reflected radiances are of the same order of magnitude during the daytime[13]. Moreover, surface-reflected solar radiance is dependent on the lower troposphere and surface properties. Thus it is possible to improve retrieval accuracy with information supplied by the surface-reflected solar beam.

This paper presents an extended version of the two-step physical retrieval algorithm (henceforth abbreviated the “extended” algorithm). The extended algorithm consists of the following four components: (i) The surface-reflected solar beam in the midwave region is directly incorporated into the retrieval; (ii) Clear-sky multitemporal (day and night) and multispectral observations[13] are combined to retrieve the atmospheric and surface parameters. (iii) The empirical orthogonal functions (EOFs)[25] technique is applied to not only atmospheric temperature-humidity profiles but also surface emissivity spectra. (iv) The retrieved atmospheric and surface parameters include daytime and nighttime temperature-humidity profile, daytime and nighttime land-surface temperature and surface emissivities in the window regions. It is assumed that the surface emissivity does not change over short durations (i.e. a few days) unless rain and/or snow occurs[15]. Section 2 describes the extended perturbation form of RTE and associated retrieved

parameter weighting functions when the surface-reflected solar beam term is included in the RTE. The solution of the RTE in the eigenvector domain is also presented. Furthermore, the improvement of retrieval accuracy is demonstrated from multitemporal and multispectral observations. Validation and error analysis of the extended algorithm are given in section 3. A more detailed discussion of the retrieval using MAS and MODIS data is included in Sections 4 and 5 respectively. Possible further improvements to the retrieval algorithm are discussed in Section 6. Finally, a conclusion is drawn in the last Section.

2. Methodology

A. Perturbation form of the radiative transfer equation

For a cloud-free atmosphere under local thermodynamic equilibrium the radiative transfer equation in the thermal infrared region may be expressed as

$$R(\nu_j,\mu) = \underbrace{B(\nu_j,t_s)\varepsilon(\nu_j,\mu)\tau(\nu_j,\mu,p_s)}_{\textit{Surface Emission Term}} - \underbrace{\int_0^{p_s}\{B[\nu_j,t(p)]\frac{f\tau(\nu_j,\mu,p)}{fp}\}dp}_{\textit{Atmospheric Emission Term}}$$

$$+\underbrace{[1-\varepsilon(\nu_j,\mu)]\int_0^{p_s}\{B[\nu_j,t(p)]\frac{f\tau^*(\nu_j,\mu,-\mu,p)}{fp}\}dp}_{\textit{Surface Atmospheric Reflected Emission Downward Term}} \qquad (1)$$

$$+\underbrace{[1-\varepsilon(\nu_j,\mu)]\alpha\tau^*(\nu_j,\mu,-\mu_0,0)(-\mu_0)\frac{E_0(\nu_j)}{\pi}}_{\textit{Surface Solar Reflected Beam Downward Term}},$$

where $R(\nu_j,\mu)$ is the mean spectral radiance measured in band j whose mean effective wavenumber is ν_j and the cosine of viewing zenith angle θ of the

observation is μ, $B(\nu_j, t_s)$ is the Planck function of surface temperature t_s, $\varepsilon(\nu_j, \mu)$ is the band-averaged surface emissivity at direction μ, and $\tau(\nu_j, \mu, p_s)$ is the transmittance from the surface pressure level p_s to the top of the atmosphere along the observation angle θ. The first term of Eq. (1) represents surface emission to space (less atmospheric absorption). The second term in Eq. (1) is the upwelling atmospheric thermal emission contribution. The third term denotes downward atmospheric thermal emission reflected back to space by the Earth's surface, where $\tau^*(\nu_j, \mu, -\mu, p) = \tau(\nu_j, \mu, p_s)\tau(\nu_j, -\mu, p_s)/\tau(\nu_j, \mu, p)$ is the reflected transmittance from surface to the pressure level p, the minus sign indicates that direction is always downward. Note that the path radiance resulting from scattering of solar radiation and the solar diffuse radiance reflected by the surface are omitted in the second and third terms, because they are much smaller than the atmospheric thermal emittance contributions in general. In the third term, the specular reflection can be expanded to general expression by considering downward atmospheric thermal irradiance. The final term represents the solar beam radiance reflected back to space by the surface, where μ_0 is cosine of the solar beam zenith angle, and $\tau^*(\nu_j, \mu, -\mu_0, 0) = \tau(\nu_j, \mu, p_s)\tau(\nu_j, -\mu_0, p_s)$ is the total transmittance for the solar beam, α is the solar BRDF factor (SBF, See Subsection 3.B.b). $E_0(\mu)$ is the solar irradiance incident on the top of the atmosphere (normal to the beam). Eq. (1) with surface-reflected solar beam term may be approximated in the numerical perturbation form[24] by

$$\delta t_B(j) = \delta t_S K^{t_s}(j) + \delta\varepsilon(j) K^{\varepsilon}(j) + \sum_{i=1}^{ls} \delta t(i) K^{t}(i, j) + \sum_{i=1}^{ls} \{\delta \ln[q(i)]\} K^{q}(i, j) , \quad (2)$$

where the perturbation δ is with respect to an a-priori estimated or mean condition, t_B is a MAS band brightness temperature vector, K^{t_S}, K^{ε}, K^{t} and K^{q} are the weighting functions of surface temperature (t_s), surface emissivity (ε), atmospheric temperature (t) and water vapor (q), respectively, i is the atmospheric quadrature pressure level ($i = 1, .. ls$, from space to surface), j denotes band number, and ls is a quadrature level of the surface pressure. For simplicity, variable μ has been omitted in the weighting functions.

Eq. (2) can be expressed in its matrix form as

$$\delta y = K \delta x \,, \tag{3}$$

where $\delta y = \delta t_B$, the weighting function matrix K contains K^{t}, K^{q}, K^{t_s} and K^{ε}, i.e.

$$K = \begin{matrix} K^{t} \\ K^{q} \\ K^{t_s} \\ K^{\varepsilon} \end{matrix}, \tag{4}$$

and

$$\delta x = \begin{bmatrix} \delta t \\ \delta \ln q \\ \delta t_s \\ \delta \varepsilon \end{bmatrix}$$

(5)

The entry $K(i,j)$, of weighting function matrix K, is expressed for temperature as

$$K^t(i,j) = \beta(i,j)\{-\frac{f\tau(i,j)}{fp(i)} + [1-\varepsilon(j)]\frac{f\tau^*(i,j)}{fp(i)}\}\delta p(i),$$

(6)

where

$$\beta(i,j) = \frac{fB[\nu_j, t(i)]/ft(i)}{fR(\nu_j,\mu)/ft_B}.$$

For water vapor,

$$K^q(i,j) = \{\beta_s(j)(t_s - t_a)\varepsilon(j)\tau_s(j) - 2[1-\varepsilon(j)]\sum_{l=1}^{ls}\beta(l,j)\tau^*(l,j)\delta t(l)$$

$$+\sum_{l=i}^{ls}\beta(l,j)\{\tau(l,j) + [1-\varepsilon(j)]\tau^*(l,j)]\delta t(l) + \frac{C[1-\varepsilon(j)]\tau_s(j)\tau_s^*(j)}{fR(\nu_j,\mu)/ft_B}\}\frac{f\ln\tau_w(i,j)}{fp(i)}\delta p(i)$$

$$+\{\frac{C[1-\varepsilon(j)]\tau_s(j)\tau_s^*(j)}{fR(\nu_j,\mu)/ft_B}\}\frac{f\ln\tau_w^*(i,j)}{fp(i)}\delta p(i),$$

(7)

For surface temperature,

$$K^{t_s}(ls, j) = \beta_s(j)\varepsilon(j)\tau_s(j),$$

(8)

and for surface emissivity,

$$K^{\varepsilon}(ls, j) = \frac{1}{fR(\nu_j, \mu)/ft_B}\{B(\nu_j, t_s)\tau_s(j) - \sum_{l=1}^{ls} B[\nu_j, t(l)]\frac{f\tau^*(l, j)}{fp(l)}\delta p(l)$$

$$- G\tau_s(j)\tau_s^*(j)\},$$

(9)

where τ_w is the water vapor component transmittance, t_a and t_s are surface air temperature (taken at 2m above ground) and surface temperature respectively, τ and τ_s represent transmittance of the atmospheric column above the level, i, and above the surface, s, respectively, for all gases, and $C = \alpha(-\mu_0)E_0(\nu_j)/\pi$. The symbol f indicates the partial derivative with respect to the vertical coordinate.

B. Solution in the eigenvector domain

Eigenvector decomposition technique[25] is widely used in retrieval. The advantages of this technique are that it reduces the number of retrieved parameters to the same order as that of measured radiances, and that it increases computational efficiency. Recently Li et.al.[26] demonstrated that surface emissivity spectra of more than 50 soil and vegetation samples measured in the laboratory can be reconstructed using six selected bands in

the 8-13 μm with an uncertainty of 0.005. The results of their study indicate that it may be possible to determine the surface emissivity spectral variations using a few surface emissivity eigenvectors. Thus in the extended algorithm the empirical orthogonal functions technique is applied to not only atmospheric temperature-humidity profiles as in the original algorithm but also to surface emissivity spectra.

Following the procedure presented by Ma et. al.[24], in the eigenvector domain the perturbation solution can be written as

$$\delta x = \sum_{i=1}^{M} f_i v_i = Vf \ , \tag{10}$$

where v_i is the ith eigenvector, f_i is the ith expansion coefficient, and M denotes the number of terms. V and f represent the eigenvector matrix and coefficient vector, respectively. The eigenvectors of atmospheric temperature and water vapor are derived from a statistical covariance matrix of a large number of atmospheric temperature and water vapor profiles. The eigenvectors of spectral emissivities are derived from an 80 surface emissivity sample dataset. And the eigenvector of surface temperature is assumed to be the unit vector. In the eigenvector domain, Eq. (3) becomes

$$\delta y = K\delta x = KVf = \hat{K}f \ . \tag{11}$$

The sounding retrieval problem has been reduced to solving a set of eigenvector expansion coefficients.

C. Combination of multitemporal and multispectral measurements

In the original algorithm, the solar contribution term was not included in the derivation of the numerical perturbation form of RTE. A sensitivity study using simulated MAS data showed that the retrieval accuracy of surface emissivities was limited, partly because the surface-reflected solar beam contribution was not included. In the extended algorithm more surface information from MODIS measurements[13,15] is utilized by including a surface-reflected solar beam term in the RTE, and by combining multitemporal and multispectral measurements in the retrieval. The surface-reflected solar beam radiances in the midwave region are an important external information source since the reflected solar contribution term in Eq. (1) is related to the surface properties and atmospheric condition in the low troposphere. In the original algorithm, a reflected sunlight model[22,27] was used to estimate the surface-reflected solar beam radiance to remove from the midwave IR measurements. It is appropriate for the removal of the solar beam contribution if surface emissivity is a known constant. However, when surface emissivity is retrieved simultaneously along with atmospheric parameters, the surface-reflected solar beam radiance provides additional information on surface properties and atmospheric status in the low troposphere (See Subsection 3.B.a). Combining daytime and nighttime measurements is also useful if surface emissivity does not change between measurements. This is probably an acceptable assumption in the absence of precipitation or vegetation change (e.g. due to fires)[15].

To evaluate the role of multitemporal and multispectral observations, the extended two-step physical retrieval algorithm was applied to day/night simulated MAS radiances. Retrieved parameters include day/night temperature-humidity profile, day/night surface temperature and surface emissivities in the window regions (MAS bands 30, 31-34, 42, and 44-46). The test data set is the same as that used for the original algorithm[24]. A set of 2512 atmospheric profiles measured by radiosonde in the period of March 2 to April 11, 1996

over the central U. S. was used as a daytime dataset. The nighttime dataset was constructed from the daytime dataset in the following way: (i) the nighttime temperature profile was generated from the daytime temperature profile by a linearly interpolated shift –6K at 1000 hPa and no change at 500 hPa; (ii) the daytime water-vapor mixing ratio profile was dried by 15% from 500-1000 hPa layer (no change above 500 hPa). The atmospheric profiles were divided into dependent (2094 profiles) and independent (418 profiles) datasets. The surface temperature was simulated for each profile from surface air temperature plus a random number with variance 4K and mean value equal to zero. The surface emissivity data, consisting of band-averaged emissivities of 80 terrestrial materials[15,24], were incorporated into the dependent and independent data. A fast regression transmittance model[28] was used to generate MAS simulated brightness temperatures for each radiosonde profile in the daytime and nighttime datasets. In the forward calculation, it is assumed that the local zenith viewing angle and solar zenith angle are 0 (nadir) and 40 degrees respectively. The solar BRDF factor is set to 1.0. Table 3.1 shows the retrieved rms of the independent dataset with the original algorithm from the daytime dataset but without the surface-reflected solar beam term (equivalent to a nighttime dataset). Table 3.2 is the same as Table 3.1 but using combined day and night simulated data. As can be seen, the retrieval accuracies of atmospheric temperature-humidity profile and surface temperature and emissivity are improved when day/night observations are used: the rms of TPW is reduced by about 30% (0.27 versus 0.34) and the rms of daytime surface temperature is significantly reduced (0.23 versus 0.49). The improvement of surface emissivity accuracy is more significant, the rms of surface emissivities in the midwave and longwave regions are 0.003 and 0.005 compared to 0.020 and 0.009 in Table 3.1. It is clearly demonstrated that the combined daytime and nighttime observations with surface-reflected solar beam radiances

directly included in the retrieval, improved the retrieval accuracies in particular for the surface emissivity in the midwave region.

3. The extended algorithm retrievals

A. Daytime/nighttime dependent and independent datasets

To demonstrate the robustness of the extended algorithm under a variety of global atmospheric conditions, 117-sounding profiles from the National Environmental Satellite, Data and Information Service (NESDIS) dataset (called Wark subset) were utilized to generate the dependent data set. The NESDIS dataset is a well-known test dataset that has 1200 profiles to comprise the complete dataset covering four seasons on the global scale. The Wark subset represents the range of meteorological conditions contained in the full dataset. An additional 40 profiles were selected from three zones (middle-latitude, high-latitude and tropical) and four seasons (Summer, Winter, Spring and Fall) in the NESDIS dataset. These profiles were used as an independent dataset. A few profiles of the independent dataset contained low level temperature inversions. For the dependent dataset, variation of surface temperature, sensor viewing zenith angle, solar zenith angle and BRDF factor for daytime are as follows: surface temperature was assigned as atmospheric air temperature t_a – 15 K to t_a + 15 K in step of 3K. Sensor viewing zenith angle varied from 0 (nadir) to 20 degrees in step of 5 degrees, and from 20 to 42 degrees in step of 2 degrees. Solar zenith angle varied from 25 to 65 degrees in step of 5 degrees and the solar BRDF factor varied from 0.85 to 1.15 in step of 0.05. These variations produced a dataset of 1,297,296 cases that should represent real atmospheric and surface variations for four seasons on the global scale. The nighttime dependent dataset was constructed from the daytime dataset following the description in Subsection 2.C. The independent dataset was generated from the 40 chosen atmospheric profiles by changing surface temperature, sensor viewing zenith angle, solar zenith angle and solar

BRDF factor randomly from their mean values. This expanded the independent dataset to 440 cases. Eighty samples of surface emissivity data spectra were randomly incorporated into the daytime/nighttime dependent and independent datasets. The surface emissivities vary from 0.56 to 0.99.

B. Sensitivity and error analysis

Forward calculations of transmittance, upwelling surface and atmospheric radiances were performed by a fast regression model[28] to obtain MAS bands 30-50 brightness temperatures for each dependent and independent case. For the daytime dataset, midwave region (bands 30-37) brightness temperatures included the surface-reflected solar radiance. An eigenvector decomposition technique was applied to the dependent dataset to describe the temperature and water vapor mixing ratio profiles. Two sets of empirical orthogonal functions were calculated; one for temperature and one for the natural logarithm of water vapor mixing ratio. Moreover, the eigenvector decomposition technique was also applied to the surface emissivity spectra dataset to generate surface emissivity eigenvectors. In the eigenvector domain, the sounding retrieval problem in the extended algorithm has been reduced to one of solving for 23 unknowns (five day/night temperature eigenvector coefficients and three day/night water vapor eigenvector coefficients, five surface emissivity eigenvector coefficients and two day/night surface temperature perturbations).

Regression analysis was then applied to the dependent dataset to generate regression coefficients relating MAS bands 30-50 brightness temperatures to the matching radiosonde temperature and water vapor profiles, surface temperature, surface emissivities and SBF. Regression retrievals were conducted with the independent simulated MAS brightness temperatures to produce a first-guess of atmospheric state and surface properties to facilitate physical solution of the RTE. A physical retrieval with a two-step algorithm[24] and iterative solution of the RTE provide the final retrievals of

temperature and water vapor profiles, surface temperature, surface emissivities.

a. Error analyses for day/night datasets versus day or night alone dataset

Table 4 lists rms values of the retrieval comparisons with the combined daytime and nighttime simulated MAS datasets versus separate daytime and nighttime datasets. The second and third columns are rms values of the combined day/night regression and two-step physical retrieval results (results for nighttime dataset are not listed). As shown, physical retrieval rms is less than that for regression retrievals. Layer Mean Temperature (LMT) 1 in the first column is the temperature profile averaged from 50 to 200 hPa. The other LMTs are averaged from 200-400, 400-600, 600-800 and 800-1000 hPa. The rms of the LMT from the regression retrieval is from 0.88-2.66K (see column 2 in Table 4) while the rms values of the extended algorithm physical retrieval is 0.84 to 2.43K. The total precipitable water vapor (TPW) rms is reduced from 0.36 to 0.25 cm. For surface properties, the rms of surface temperature and surface emissivities are reduced significantly. Especially for surface emissivities in the midwave region, accuracy improvement is much more prominent (50-66% reduction). Histograms of extended algorithm retrieval bias (true – retrieval) in surface temperatures are shown in Figure 1, where the left-hand (right-hand) panel is for daytime (nighttime). Figure 2 is the same as Figure 1 but for TPW. As shown, the errors are within 0.5K for surface temperature and 0.5cm for TWP in most of cases. Figure 3 is the same as Figures 1 and 2, but for retrieved surface emissivities. The upper two panels represent biases in window bands 31 (left-hand) and 32 (right-hand) emissivities; the bottom two panels are in window bands 44 and 45 emissivities. The range of bias is within 0.01. Columns 4 and 5 in Table 4 represent the rms values of regression and physical retrievals with the

daytime dataset alone. Columns 6 and 7 show the rms values for the same dataset when the surface-reflected solar beam contribution is removed. It is equivalent to a nighttime dataset. As shown in columns 4 and 5 in Table 4, physical retrieval rms values of all retrieved parameters are smaller than those generated from regression retrieval although the improvements are not as large as those with the combined daytime and nighttime datasets. However, the accuracy of retrieved surface emissivities was not improved for the nighttime alone dataset. These error analyses show that the extended physical algorithm using combined daytime/nighttime observations and retaining the surface-reflected solar beam term is able to retrieve atmospheric and surface properties simultaneously with much better retrieval performance.

b. Sensitivities to the uncertainties in solar BRDF factor

It's assumed that a single BRDF factor[15] can be used for the surface-reflected solar beam within the midwave region. The SBF α is defined as follows:

$$\alpha = \frac{\pi f_r(\mu; -\mu_0, \varphi_0)}{r},$$

where r is reflectance of the assumed Lambertian surface. $f_r(\mu; -\mu', \varphi')$ is the BRDF, where the cosine of local zenith angle θ of the observation is μ, $-\mu'$ and φ' represent solar beam incident direction (the minus sign indicates downwelling). In the retrieval, the SBF is obtained from regression analysis, then this value is directly used in physical processing due to lack of a simple and accurate physical model to estimate the solar BRDF factor. By doing this, it would bring 0.05 rms error of SBF (regression SBF vs. true SBF) into the physical retrieval processing. Thus the uncertainties in SBF would degrade the retrieval performance. Table 5 summarizes error analysis results, where column 2 represents the rms departure of the independent dataset cases

from the mean profile of the dependent dataset, and column 3 is the rms in the regression retrieval. Column 4 indicates the rms of the extended physical rms in the regression retrieval. Column 4 shows the rms values of the extended physical retrieval under conditions: (i) no noise was added; (ii) regression guess SBF was used; (iii) surface emissivity spectrum unvaried from daytime to nighttime. Column 5 shows the rms values when a true SBF was used. It illustrates that rms values of retrieved parameters almost do not vary with an uncertainty range of 0.05 in SBF (columns 4 versus 5), except some small changes in the retrieved midwave emissivities.

c. Sensitivities to instrument noise and co-registration error

The MAS instrument noise can be described statistically as having a Gaussian probability distribution with a mean of zero and a spectrally varying standard deviation referred to as the noise equivalent temperature difference NEDT (K). Also, when clear-sky day/night observations are combined to retrieve atmospheric and surface properties, there may be an error in day/night registration. The day/night registration error can be reduced by using surface features to adjust the day/night registration. Investigation was conducted to estimate how MAS instrument noise and co-registration error influence retrieval results. A random noise of 0.2K was added into MAS bands 30-50 to simulate uncertainties arose from MAS instrument noise, co-registration error, and other error sources such as the forward model calculation error. The rms results are given in column 6 of Table 5. Statistical comparisons between the values in columns 6 and 4 show that as noise is added the accuracy of the retrieval is slightly degraded but it is still quite good. The accuracy of retrieved atmospheric temperature profile and surface temperature degrade by less than 0.1K. TPW degrades less than 0.1cm. Retrieved surface emissivities degrade less than 0.3%. It indicates

that the extended physical retrieval algorithm is not highly sensitive to instrument noise, co-registration error, and other error sources.

d. Sensitivities to the uncertainties in surface emissivities

In the extended algorithm with day/night observations it is assumed that surface emissivities remain unchanged from daytime to nighttime. However, it is possible that the night surface emissivity changes with surface moisture. Thus some variations for the nighttime surface band emissivities are introduced to simulate the emissivity variation. A nighttime surface band emissivity was regenerated from a daytime surface emissivity plus a random number with mean of zero and variance 0.01. The rms of retrieved parameters is summarized in the final column of Table 5. As shown, improvements of atmospheric and surface parameters are mitigated as surface band emissivities vary from daytime to nighttime (columns 4 versus 7). But it is still better than regression retrieval as long as the emissivity variation is small.

4. Application to MAS real observations

The extended algorithm was applied to MAS real data collected during the WINter Experiment (WINTEX)[29]. WINTEX was conducted in Madison, Wisconsin from March 15 to April 2 making measurements from a NASA ER-2 to define the measurement requirements for the next generation of the National Polar Orbiter Environmental Satellite System and to further global climate study. During ER-2 flight #99-051 (18 March, 1999), MAS clear sky data scenes were collected over Madison in Wisconsin. Three minutes of data (1000 scans, ~40 km X 35 km) from 21:13 to 21:16 UTC were selected to test the extended algorithm. The WINTEX home page (http://asapdata.arc.nasa.gov/WINTEX_home.html) provides MAS browse image and flight information for the ER-2 flight track for 18 March, 1999 (20:00-22:00 UTC). The MAS 50 m resolution image contained 1000 lines with 716 pixels per line. The MAS data were averaged on 10x10 pixels. The

average processing reduced the image size to 70 large pixels per a line by 100 lines (See Fig. 4). Unfortunately, there were no ER-2 flights in the week following 8 March, so only daytime MAS data were utilized to validate the extended algorithm. We used 1471 sounding profiles from the period of 1 February to 5 March, 1999 over the central and eastern U. S. and Canada to develop coefficients for the regression first-guess. Following the same procedure in Subsection 3.A, the nighttime dependent dataset was created. To better represent surface types in the Madison area, some material samples such as minerals and rocks were excluded from the MAS band averaged surface emissivity database. The mean solar zenith angle used to calculate solar beam contributions was 66.88 degrees. A set of regression coefficients that relate retrieved parameters (atmospheric temperature-humidity profile, surface temperature, surface emissivities and SBF) to the MAS simulated brightness temperature was generated from the dependent dataset. Surface pressure and sensor viewing angle were added as additional predictors to account for in the real observations. Empirical orthogonal functions were calculated for the dependent dataset to generate temperature, water vapor, and surface emissivity eigenvectors.

The extended algorithm uses surface-reflected solar beam radiances to improve retrieval of lower troposphere and surface properties. Thus it is important to accurately estimate surface-reflected solar beam radiances over different types of land cover. Figure 4 shows the image of MAS band 7 (in visible region) reflectance data. The dark (low reflectance) areas on the image are Lakes Mendota, Monona, Waubesa and Kegonsa in sequence of from upper left to lower right. As shown, open water and ice contrast sharply to land. To validate this observation, two MAS pixels were chosen, one over Lake Mendota and the other over nearby land. Their brightness temperatures are listed in Table 6. The brightness temperature in band 45 is ~ 7K colder over open water than land, while the band 30 brightness temperature difference

approaches 15K. Thus it is necessary to generate separate sets of regression coefficients for different surface types. No solar beam contribution was considered in the midwave region for MAS pixels in open water and ice-coved lake. Namely the effect of solar beam contributions over open water was neglected. When regression retrieval was implemented at each MAS pixel, the reflectance value in MAS band 7 was used in a test to distinguish open water (< 0.8) from land (? 0.8). Figure 5 shows retrieved surface emissivity for bands 45 (the left-hand panel) and 46 (the right-hand panel). Emissivity ranges from 0.95 to 1.0. Figure 6 shows results for bands 31 (the left-hand panel) and 32 (the right-hand panel). Obviously, the surface emissivity in the midwave region varies in a larger range (from 0.9 to 1.0). It is desirable to compare the retrieved surface emissivities with measured emissivity spectra[30-31]. However, these comparisons are of limited value since the measured emissivity spectra are for specific terrestrial materials only, e.g. tap water, ice, a specific tree, soil, rock, etc. Surface emissivity depends on the surface composition (soil, vegetation, snow, wetness, etc.) and geometry (soil roughness, geometry of the vegetation canopy, topography, etc.). Real surfaces often consist of several mixed terrestrial materials except when snow cover is present. For this reason, comparisons were limited to the Lake Mendota and other lake scenes; it was independent observed that ~75% surface of Lake Mendota was ice covered on 18 March, while the other lakes were entirely open water. The measured and retrieved emissivity values in MAS bands 31, 32, 45 and 46 are summarized in Tables 7.1 and 7.2. As shown in Figures 5 and 6, retrieved water emissivity is slightly higher in band 32 than band 31, and in band 45 than band 46. This agrees with measurement values given in Table 7.1. The emissivity retrieved over ice (Lake Mendota) is almost identical (approximately 0.98) for bands 31 and 32, but it is higher in band 45 (~0.98) than 46 (~0.96). One can see some variations in the retrieved emissivity over Lake Mendota because it was partly covered by ice.

Furthermore, Figure 7 provides a comparison of retrieved surface emissivities in band 31 (the left-hand panel) and band 46 (the right-hand panel). The retrieved surface emissivity over water (ice) is higher (lower) for band 46 than band 31. Again this is consistent with the measured results. Therefore, the extended algorithm did well in retrieving surface emissivities over open water and ice. Surface emissivity over land requires further investigation.

Figure 8 shows retrieved land-surface temperature. The retrieved surface temperature ranges from 272K (lake scenes) to 289 K (urban cover). Surface temperature of Lake Mendota is a few K colder than the other lakes since 75% Lake Mendota was ice covered. Note that there is a strip of warmer surface temperature between Lakes Mendota and Monona in the image. This is downtown Madison, a highly urbanized region. Much of the snow cover has been removed in this strip. Figure 9 shows a retrieved atmospheric temperature-humidity profile compared with a collocated AERI (Atmospheric Emitted Radiance Interferometer)-GOES retrieved profile. The solid curve represents the retrieval results from the extended algorithm. The dotted-dashed curve represents regression retrieval. The dashed curve is the AERI-GOES retrieved profiles (the time difference between MAS and AERI-GOES is less than 10 minutes). The AERI is a ground-based passive infrared observation system that provides 10-min temporal resolution atmospheric emitted radiance spectra of better than one wavenumber in spectral resolution. The AERI has demonstrated a capability of retrieving thermal and moisture vertical structure in the lowest 3 km of the Earth's atmosphere[32-34]. Combined AERI-GOES retrievals take advantage of up-looking and down-looking emission measurements. Satellite based GOES measurements are best suited for temperature-humidity vertical structure in the upper and mid-troposphere, while ground-based AERI excels at providing thermal and moisture information in the planetary boundary layer (PBL). In the left-hand panel of Fig. 9, the extended algorithm retrieved temperature profile is almost exactly the same as the regression retrieval

(only 0.1-0.2K better at low troposphere). This indicates that the physical retrieval is not able to improve temperature retrieval accuracy. The MAS and AERI-GOES temperature retrievals in Fig. 9 show a large discrepancy of almost 10 K near the tropopause (~200 hPa). This on large part is traceable to the MAS first-guess regression retrieval, which has difficulty resolving the tropopause temperature. By contrast, the National Centers for Environmental Prediction (NCEP) 6- to 18-h forecast from the Nested Grid Model[35] is adopted as a first-guess profile in the GOES retrieval. The discrepancy between the guess temperature profile and rawinsonde observation (RAOB) can reach as small as 1-2K. Thus GOES retrieval benefits from the accurate guess profile. In the AERI retrieval first-guess profile is obtained from regression analysis, similar to the MAS retrieval. However, the radiosonde climatology data were collected in a small region for AERI retrieval so that a good regression first-guess can be achieved (the rms differences between regression first-guess and RAOB is within 1-2K[33]). MAS water vapor retrieval is much better than temperature retrieval (right-hand panel of Fig. 9). The physical retrieval made a significant improvement for TPW with MAS data. The water vapor regression first-guess is too wet compared to AERI-GOES retrieval result. The physical retrieval made it drier based on water vapor information provided by MAS bands 40-42. The TPW values from regression and physical retrievals are 0.86 and 0.58 respectively, while the TPW from AERI-GOES retrieval is 0.50. The retrieved bias is reduced from 72% to 16%.

5. Application to MODIS real observations

The extended algorithm was also applied to MODIS real observations. The daytime data set (descending overpass) was selected at 17:00-17:05 UTC on 17 September, 2000, and the nighttime data set (ascending overpass) at 04:05-04:10 UTC next day. The MODIS calibrated radiance level-1B (L1B) data granule has 2030 scan lines with 1354 pixels per line. The daytime/nighttime datasets

have an overlapped area over central and eastern U. S. (Figure 10). Only 1900 lines are shown in Figure 10 since there are some missing data lines in the beginning of the daytime L1B data. The left-hand (right-hand) panel in Figure 10 is the image of daytime (nighttime) brightness temperature in MODIS band 32. We used MODIS datasets including calibrated radiances in L1B data product (version 2.4.3), and latitude/longitude, sensor local zenith angle, solar zenith angle, land/water flag, and clear/cloud scene information in the corresponding geo-location and cloud mask data products. The MODIS bands used for retrieval performance evaluation are bands 20, 22-25 and 27-36 respectively.

A. Data pixel registration

It is a crucial step to register pixels in the daytime and nighttime datasets with a minimum registration offset so that the sensor views the same geophysical location. The registration is accomplished by mapping the daytime/nighttime data into standard map grids (resolution 10 km). The map-grid adopted here is an equal-area grid since the equal-area grid maintains approximately equal statistical significance[36]. So it would be more appropriate for the aggregation of radiance data. First, pixels with cloud flags or brightness temperatures out of reasonable ranges were excluded. Second, daytime/nighttime data were mapped into equal-area grids and the number of pixels was counted in each grid. If the number of clear pixels in a grid is less than 5, then this grid is discarded. Latitude/longitude, sensor local zenith angle, solar zenith angle, corresponding to clear-sky pixels were also averaged. The land flag was set to 1 (0) if more (less) than 50% pixels within a grid were over land. Finally, daytime and nighttime band brightness temperatures were averaged in 10x10 km grids. Figure 11 shows the collocated

daytime/nighttime images of band 32 brightness temperatures at 10x10km grids. Lakes Michigan, Huron and Erie are shown in both daytime and nighttime images.

B. Regression and physical retrievals

Regression and physical retrievals were applied to the collocated daytime/nighttime datasets. Since MODIS overpass times are not close to the synoptic time (0 or 12 UTC), the GOES retrieval results instead of RAOB data were used for comparison. There are two options to choose the first- guess for physical retrieval, option 1 is from regression method and option 2 is to use the GOES first-guess. It is better to use the GOES first-guess to evaluate the performance of the extended algorithm because it would be much comparable if the same first-guess was used for both retrievals. However, the GOES first-guess could not be used directly for MODIS retrieval due to different spatial resolutions. For instance, there are 1574 temperature and water vapor guess profiles with GOES for the daytime dataset, while 19682 profiles are needed for the grids in the MODIS retrieval. Hence for each MODIS retrieval, a MODIS first-guess was generated using a linear interpolation method based on the nearest GOES FOVs. The generated MODIS first-guess has resemblance to the GOES first-guess. For the first-guess of surface temperature and emissivities, the regression results were used. So the MODIS first-guess is a hybrid first-guess including temperature-humidity profile from the GOES first-guess and surface temperature and emissivities from the regression results. Figure 12 shows the retrieved surface temperature from MODIS data. The upper (bottom) panel is for the daytime (nighttime). Note that the white dots or curves or areas in the images indicate no retrieval result available. The diurnal variation of surface temperature over land is clearly shown. The surface temperature is much colder at night than in day over land, while surface temperature over open water varies much smaller. Figure 13 is the surface temperature retrieved from GOES

data and displayed at the MODIS retrieval grids for a better comparison. The GOES retrieved surface temperature (Figure 13) and TWV (figure 15) images were generated from the GOES retrieved results, if no GOES retrieval results exists at the MODIS retrieval grid, a value was selected from the GOES dataset at the nearest distance. As shown, a good agreement is achieved between two images in Figures 12 and 13, higher (lower) surface temperature areas are matched well. However, the retrieved daytime surface temperature at the left-bottom area in the MODIS image (upper panel) is probably 1-2K higher than that in the GOES image. One of the reasons to explain the discrepancy might be the difference in their retrieval algorithms. In the extended algorithm, surface temperature and emissivity along with atmospheric temperature-humidity profile are retrieved simultaneously. In the GOES physical retrieval algorithm, a sequential method is used to deal with the surface emissivity[22]. Since there were no GOES sounding data available at 04:00 UTC on 18 September, the dataset at 03:00 UTC was used for the nighttime surface temperature comparison (bottom panels). Figures 14 and 15 are the same as for Figures 12 and 13, but for the retrieved total precipitable water vapor (TWV). The wettest grids (~4.0 cm) in the MODIS image on the upper panel of Figure 14 cannot be found in Figure 15 of the GOES retrieval results because there are no GOES retrieval results available at these grids due to clouds. Except that, the TWV distribution retrieved from MODIS data is similar to the GOES retrieval result. The validation of the retrieved surface emissivities in band 22 (in the midwave window) and band 32 (in the longwave window) was limited to Lake Michigan. The retrieved surface emissivities are approximately 0.97 and 0.98 in these two bands, which are close to the measured values in Table 7.1. In summary, the performance of extended algorithm was evaluated by comparing the retrieved results from MODIS data with the GOES retrieval result. It demonstrates that the extended algorithm is capable of retrieving medium-scale atmospheric

temperature/water vapor and surface temperature/emissivity with similar retrieval accuracies as GOES achieves plus much higher spatial resolution.

6. Possible further improvements

Physical retrieval algorithms, including the extended algorithm presented in this paper, benefit from a good first-guess profile. With the NCEP NGM[37] output as first guess, the GOES retrieval provides higher spatial and temporal resolution moisture information beyond that of conventional radiosondes[35]. Thus using a model-based first-guess for the MODIS retrieval also improves moisture retrieval as demonstrated in Section 5. Another first-guess option is to take advantage of the AIRS retrieval. The high spectral resolution of AIRS produces sharp vertical weighting functions and minimizes the contamination of temperature sounding with water vapor lines and other atmospheric gases. AIRS, together with the Advances Microwave Sounder unit (AMSU) and the Microwave Humidity Sounder supplied by Brazil (HSB) is expected to obtain global temperature-humidity profile with much higher accuracy at coarser spatial resolution. The retrieval accuracy for temperature and humidity are 1K rms in 1km thick layers and 10% rms in troposphere respectively. The second MODIS, AIRS, and other sounders will be flown together on the EOS PM-1 platform (to be launched in 2001). The retrieved temperature-humidity profile and surface temperature from AIRS data can be used as a first-guess in the MODIS retrieval. Due to its higher spatial resolution (1km at nadir for MODIS versus 15km for AIRS in the infrared region), more spatial variations in atmospheric thermal structure and humidity distribution as well as surface parameters could be retrieved from MODIS data. Moreover, MODIS data provide more detailed cloud information in the FOV of AIRS and cloud information is crucial to obtain better retrieval results.

The first guess of surface emissivities is another important factor for the performance of physical retrieval algorithms. The temperature independent

spectral index based day/night method[13-14] may provide a better first-guess of land-surface emissivities. In cases of spectral/spatial surface emissivity variation, accounting for this variation will improve the accuracy of retrieved atmospheric profiles[23]. Multiple end-member spectral mixture models[38,39] may provide useful information to infer emissivity. A better first guess of surface emissivity may be obtained by a combined use of MODIS visible, near-infrared, and thermal infrared data through a synergism of BRDF models in visible near-infrared[40-41] and thermal infrared[42] regions.

7.Conclusion

An extension to the two-step physical algorithm has been presented in this paper. The extended algorithm retrieves day/night atmospheric temperature-humidity profile, day/night land-surface temperature and emissivities in the atmospheric window regions simultaneously from combined day/night MODIS observations. The solar contribution term has been included in the linear perturbation of RTE. The surface-reflected solar beam radiance within the midwave region is an additional source to improve retrieval accuracy in lower troposphere and surface properties. Simulation study has demonstrated that retrieval performance is greatly improved when the combined day/night observations are used. Sensitivity study and error analysis also indicate that the extended algorithm is relatively insensitive to instrument noise, co-registration error between multitemporal observations, surface emissivity variation during the day/night period and the SBF uncertainty. The extended algorithm was applied to MAS real observations from NASA ER-2 aircraft over Madison, WI during the WINTEX campaign. The retrieved surface emissivities within the window regions were obtained. Good agreements between retrieved and measured surface emissivities of water and ice surfaces were achieved. Along with retrieved surface emissivities, surface temperature and atmospheric temperature-humidity profile were also retrieved simultaneously. Retrieved

TPW was verified against AERI-GOES results. The TPW bias is reduced from 72% to 16%. Furthermore, the extended algorithm was also applied to real MODIS day/night observations illustrating that it is capable of retrieving medium-scale atmospheric temperature/water vapor and surface temperature/emissivity with similar retrieval accuracies as GOES achieves plus much higher spatial resolution. With the MODIS data collected from the EOS AM platform (named Terra) and to be collected from the EOS PM platform (named Aqua) in the near future, the extended day/night method will provide better diurnal information of the global atmospheric and surface information at a moderate spatial resolution of 5-10km.

7. Acknowledgements

We would like to thank H. M. Woolf for his dedicated contributions to the MAS and MODIS transmittance model development, calculation and collecting all RAOB data used in this study. Authors also thank T. J. Schmit and T. Schreiner for their valuable comments and suggestions, and K. Strabala for providing the MAS cloud mask source code. Our thanks are also extended to Richard Frey for using his subroutine to collocate day/night datasets, B. Howell and G. Bayler for providing AERI-GOES and GOES first-guess and retrieved datasets. This research is supported by EOS program contracts NAS5-31370 and NAS5-3131367 of NASA.

References

1. L. M. McMillin, “Estimation of sea surface temperatures from two infrared window measurements with different absorption,” J. Geophys. Res., **80**, 113-5117 (1975).

2. L. M. McMillin and D. S. Crosby, “Theory and validation of the multiple window sea surface temperature technique,” J. Geophys. Res., Vol. **89**, 3655-3661 (1984).

3. C. C. Walton, “ Nonlinear multichannel algorithms for estimated sea surface temperature with AVHRR satellite data,” J. Appl. Meteorol., **27**, 115-124 (1988).

4. C. C. Walton, E. P. McClain, and J. F. Sapper,“ Recent changes in satellite-based multichannel sea surface algorithms,” Rep. MTS **90**, Mar. Technol. Soc., Washington, D. C. (1990).

5. N. R. Nalli and W. L. Smith, “Improved sensing of sea surface skin temperature using a physical retrieval method,” J. Geosci. Res., **103**, 10527-10542 (1998).

6. Z. Wan and J. Dozier, “Land-surface temperature measurement from space: physical principles and inverse modeling,” IEEE Trans. Geosci. Remote Sens., **27**, 268-277 (1989).

7. J. C. Price, “Land surface temperature measurements from the split window channels of the NOAA-7 AVHRR,” J. Geophys. Res., **79**, 5039-5044 (1984).

8. F. Becker and Z.-L. Li, “Toward a local split window method over land surface,” Int. J. Remote Sens., **11**, 369-393 (1990).

9.Y. H. Kerr, J. P. Lagouarde, and J. Jmbernon, “Accurate land surface temperature retrieval from AVHRR data with use of an improved split window algorithm,” Remote Sens. Environ., **41**, 197-209 (1992).

10. A. J. Prata, “Land surface temperature derived from the advanced very high resolution radiometer and the along-track scanning radiometer 2. Experimental results and validation of AVHRR algorithms,” J. Geophys. Res., **99**, 13025-13058 (1994).

11. Z. Wan and J. Dozier, “A generalized split-window algorithm for retrieving land-surface temperature from space,” IEEE Trans. Geosci. Remote Sens., **34,** 892-905 (1996).

12. Z. Wan, “Estimate of noise and systematic error in early thermal infrared data of the Moderate Resolution Imaging Spectroradiometer (MODIS),” Remote sens. Environ., submitted 2001.

13. Z.-L. Li and F. Becker, “Feasibility of land surface temperature and emissivity determination form AVHRR data,” Remote Sens. Environ., **43**, 67-85 (1993).

14. Z.-L. Li, F. Petitcolin, and R. Zhang, “A physically based algorithm for land surface emissivity retrieval from combined mid-infrared and thermal infrared data,” Science in China (Series E), **43**, 23-33, 2000.

15. Z. Wan and Z. L. Li, “A physics-based algorithm for retrieving land-surface emissivity and temperature from EOS/MODIS data,” IEEE trans. Geosci. Remote Sens., **35,** 980-996 (1997).

16. W. L. Smith, H. M. Woolf, and A. J. Schriener, “Simultaneous retrieval of surface and atmospheric parameters: a physical and analytically direct approach,” in *Advances in Remote Sensing Retrieval Method*, A. Deepak, H. E. Flemming and M. T. Chahine, eds (Deepak, Hampton, Va., 1985), pp. 221-232.

17. W. L. Smith, H. M. Woolf, H. B. Howell, H.-L. Huang, and H. E. Revercomb, “The simultaneous retrieval of atmospheric temperature and water vapor profiles – application to measurements with the high spectral resolution interferometer sounder (HIS),” in *Advances in Remote Sensing Retrieval*

Methods, A. Deepak, H. E. Flemming, and J. S. Theon, eds. (Deepak, Hampton, Va., 1989), pp. 189-202.

18. W. L. Smith, H. E. Revercomb, H. B. Howell, H.-L. Huang, R. O. Knuteson, E. W. Koenig, D. D. LaPorte, S. Silverman, L. A. Sromovsky, and H. M. Woolf, "GHIS – The GOES high – resolution interferometer sounder," J. Appl. Meteor., **29,** 1189-1204 (1990).

19. W. L. Smith, H. M. Woolf, and H. E. Revercomb, "Linear simultaneous solution for temperature and observing constituent profiles from radiance spectra," Appl. Opt. **30,** 1117-1123 (1991).

20. W. L. Smith, H. M. Woolf, C. M. Hayden, and A. J. Schreiner, "The simultaneous retrieval export package," presented at the Second International TOVS Study Conference. lgls, Austria, 18-22 February (Cooperative Institute for Meteorological Satellite Studies, University of Wisconsin-Madison, Madison, Wis., 1985), pp. 224-253.

21. H.-L. Huang, "An analysis of the characteristics of the atmospheric profiles obtained with the High-resolution Interferometer Sounder (HIS)," Ph.D. dissertation (University of Wisconsin-Madison, Madison, Wis., 1989).

22. C. H. Hayden, "GOES-VAS simultaneous temperature-moisture retrieval algorithm," J. Appl. Meteorol. **27**, 705-733 (1988).

23. Y. Plokhenko and W. P. Menzel, "The effects of surface reflection on estimating the vertical temperature-humidity distribution from spectral infrared measurements," J. Appl. Meteorol. **39**, 3-14 (2000).

24. X. L. Ma, Z. M. Wan, C. C. Moeller, W. P. Menzel, L. E. Gumley, and Y. L. Zhang, “Retrieval of geophysical parameters from Moderate Resolution Imaging Spectroradiometer thermal infrared data: evaluation of a two-step physical algorithm,” Appl. Opt. **39**, 3537-3550 (2000).

25. W. L. Smith and H. M. Woolf, “The use of eigenvectors of statistical covariance matrices for interpreting satellite sounding radiometer observations,” J. Atmos. Sci., **33**, 1127-1140 (1976).

26. Z.-L. Li, F. Becker, M. P. Stoll, Z. Wan, and Y. Zhang, “Channel selection for soil spectrum reconstruction in 8-13 μm region,” J. Geophys. Res. **104**, 22271-22285 (1999).

27. W. L. Smith, H. M. Woolf, P. G. Abel, C. M. Hayden, M. Chalfant, and N. Grody, “NIMBUS-5 Sounder Data Processing System, Part 1: Measurement Characteristics and Data Reduction Procedures,” NOAA Tech. Memo. NESS **57**, (Notional Oceanic and Atmospheric Administration, Washington, D. C., 1974), pp. 36-41.

28. H. M. Woolf, P. V. Delst, and W. J. Zhang, “NOAA-15 HIRS/3 and AMSU transmittance model validation”, in Proceeding of the Tenth International TOVS Study Conference, Boulder, Co. 27 Jan. – 2 Feb. 1999, (Bureau of Meteorology Research Center, Melbourne, 1999), pp. 564-573.

29. W. Smith, A. Larar, D. Zhou, C. Sisko, J. Li, B. Huang, H. Howell, H. Revercomb, D. Cousins, M. Gazarik, D. Mooney, and S. Mango, “NAST-I: Results from Revolutionary Aircraft Sounding Spectrometer,” Denver, Co., July 1999, SPIE Conference on Optical Spectroscopic Techniques and Instrumentation for Atmospheric and Space Research III, pp. 2-8.

30. J. W. Salisbury and D. M. D'Aria, "Emissivity of terrestrial materials in the 8-14 μm atmospheric window," Remote Sens. Environ., Vol. **42**, 83-106 (1992).

31. J. W. Salisbury and D. M. D'Aria, "Emissivity of terrestrial materials in the 3-5 μm atmospheric window," Remote Sens. Environ., Vol. **47**, 345-361 (1994).

32. W. L. Smith, W. F. Feltz, R. O. Knuteson, H. E. Revercomb, H. M. Woolf, and H. B. Howell, " The retrieval of planetary layer structure using ground-based infrared spectral radiance measurements," J. Atmos. Ocean. Tech., **16**, 323-333 (1999).

33. W. F. Feltz, W. L. Smith, R. O. Knuteson, H. E. Revercomb, H. M. Woolf, and H. B. Howell, " Meteorological applications of temperature and water vapor retrieval from the ground-based atmospheric emitted radiance interferometer (AERI)," J. Appl. Meteorol. 37, 857-875 (1999).

34. T. J. Schmit, W. F. Feltz, W. P. Menzel, J. Jung, J. P. Nelson III, and G. S. Wade, " Validation and use of GOES sounder moisture information", submitted to the Bull. Ameri. Meteorol. Soc. (2000).

35. X. L. Ma, T. J. Schmit, and W. L. Smith, "A non-linear physical retrieval algorithm – its application to the GOES-8/9 sounder," J. Appl. Meteor., **38,** 501-513 (1999).

36. W. B. Rossow and L. C. Garder, "Selection of a map grid for data analysis and archival," J. Climate Appl. Meteor., **23**, 1253-1257 (1984).

37. J. E. Hoke, N. A. Phillips, G. J. DiMego, J. J. Tuccillo, and J. G. Sela, “The regional analysis and forecast system of the National Meteorological Center,” Wea. Forecasting, **4**, 323-334 (1989).

38. T. H. Painter, D. A. Roberts, R. O. Green, and J. Dozier, “The effects of grain size on spectral mixture analysis of snow-covered area from AVIRIS data,” Remote Sens. Environ., **65**, 320-332 (1998).

39. D. A. Roberts, M. Gardner, R. Church, S. Ustin, G. Scheer, and R. O. Green, “Mapping chaparral in the Santa Monica mountains using multiple endmembers spectral mixture models,” Remote Sens. Environ. **65**, 267-279 (1998).

40. L. J. Roujean, M. Leroy, and P. Y. Deschamps, “A bi-directional reflectance model of the Earth’s surface for the correction of remote sensing data,” J. Geophys. Res., **97**, 445-468 (1992).

41. W. Wanner, A. H. Strahler, B. Hu, P. Lewis, J.-P. Muller, X. Li, C. Barker-Schaaf, and M. Barnsley, “Global retrieval of bi-directional reflectance and albedo over land from EOS MODIS and MISR data: theory and algorithm,” J. Geophys. Res.-Atmos., **102**, 17143-17161 (1997).

42. W. C. Synder and Z. Wan, “BRDF models to predict spectral reflectance and emissivity in the thermal infrared,” IEEE Trans. Geosci. Remote Sens., **36**, 214-225 (1998).

List of Figures

1. The histograms of extended algorithm retrieval bias in surface temperature (T_s). The left-hand panel is for daytime dataset and the right-hand panel is for nighttime dataset.

2. Same as Fig. 1, but for total precipitable water vapor (TWV).

3. The histograms of extended algorithm retrieval bias for surface emissivities. The upper two panels are for MAS bands 31 (left-hand) and 32 (right-hand) respectively. The bottom two panels are for MAS bands 44 (left-hand) and 45 (right-hand) respectively.

4. MAS visible band 7 reflectance on 18 March, 1999 (21:13-21:16 UTC) over Madison, Wisconsin.

5. MAS bands 45 (left-hand panel) and 46 (right-hand panel) surface emissivity images retrieved from the MAS real observations.

6. Same as Fig. 6, but for MAS bands 31 (left-hand panel) and 32 (right-hand panel).

7. MAS bands 31 (left-hand panel) and 46 (right-hand panel) surface emissivity images retrieved from the MAS real observations on 18 March, 1999 (21:13-21:16 UTC) over Madison, Wisconsin.

8. Surface temperature (in Kelvin) image retrieved from the MAS real observation on 18 March, 1999 (21:13-21:16 UTC) over Madison, Wisconsin.

9. Temperature and water vapor mixing ratio retrieval comparisons with AERI-GOES retrieval results.

10. MODIS daytime (left-hand panel) and nighttime (right-hand panel) band 32 image at 10x10km grids on 17 (17:00-17:05 UTC) and 18 (04:05-04:10 UTC) September, 2000.

11. Same as Fig. 10, but for the collocated daytime (upper panel) and nighttime (bottom panel) datasets at 10x10km grids.

12. Daytime (upper panel) and night (bottom panel) surface temperature (in Kelvin) image retrieved from the MODIS real observations on 17 (17:00-17:05 UTC) and 18 (04:05-04:10 UTC) September, 2000.

13. Same as Fig. 12, but for retrieved from the GOES real observations on 17 (17:00 UTC) and 18 (03:00 UTC) September, 2000. The image was generated from the GOES retrieved dataset but displayed at the retrieval grids.

14. Same as Fig. 12, but for retrieved total precipitable water vapor (in centimeter).

15. Same as Fig. 13, but for retrieved total precipitable water vapor (in centimeter).

Table 1, Spectral characteristics of the MODIS

TIR bands

MAS band	Central wavelength (μm)	Bandwidth (μm)	NEDT[a](K)		Primary use
			Specified	Estimated	
20	3.79	0.19	0.05	0.21	L
21	3.99	0.08	2.00	1.07	F
22	3.97	0.09	0.07	0.19	L, O
23	4.06	0.09	0.07	0.18	L
24	4.47	0.09	0.25	0.31	A
25	4.55	0.09	0.25	0.27	A
27	6.77	0.24	0.25	0.73	A
28	7.33	0.33	0.25	0.63	A
29	8.54	0.37	0.05	0.18	A, L
30	9.73	0.30	0.25	0.36	Ozone
31	11.01	0.52	0.05	0.17	A, L, O
32	12.03	0.52	0.05	0.17	A, L, O
33	13.36	0.31	0.25	0.35	A
34	13.68	0.33	0.25	0.45	A
35	13.91	0.33	0.25	0.36	A
36	14.20	0.29	0.35	0.61	A

[a] Noise Equivalent Temperature Differences (NEDT) for bands 20-36 were estimated with the 17 September dataset over Lake Michigan. They are larger than specifications. A recent study[12] shows the NEDT specifications are achieved in the most bands.

Note:

A atmospheric studies L land studies

C cirrus cloud O ocean studies

F fire

Table 2, Spectral characteristics of the MAS

TIR bands in its 1999 configuration

MAS band	Central wavelength (μm)	Bandwidth (μm)	NEDT[a](K)	Primary use
30	3.75	0.16	1.36	L
31	3.92	0.15	1.02	L,O
32	4.07	0.17	1.09	L
33	4.23	0.16	2.87	L
34	4.38	0.16	3.46	L
35	4.54	0.15	0.75	A
36	4.70	0.16	0.49	A
37	4.85	0.16	0.38	A
38	5.00	0.16	0.31	A
39	5.16	0.15	0.54	A
40	5.30	0.16	0.34	A
41	5.39	0.16	1.06	A
42	8.48	0.44	0.09	A, L
43	9.67	0.62	0.13	Ozone
44	10.44	0.49	0.09	A, L
45	10.95	0.54	0.07	A, L,O
46	11.94	0.45	0.25	A, L,O
47	12.82	0.46	0.41	A, L
48	13.22	0.47	0.59	A
49	13.76	0.60	1.81	A
50	14.22	0.42	4.18	A

[a] Noise Equivalent Temperature Differences (NEDT) for bands 30-50 were estimated with 25 March 1999 data over Lake Superior.

Note:

A atmospheric studies

L land studies

O ocean studies

Table 3.1. Retrieval rms of the independent dataset simulated for 418 daytime cases, with solar contribution removed and no noise added

Layer(hPa)[a]	Dep. mean profile	Regression rtvl.	Physical rtvl.
1 (50-200) T_a (K)	4.46	1.04	0.89
2 (200-400) T_a (K)	3.32	1.49	1.42
3 (400-600) T_a (K)	5.62	1.26	1.14
4 (600-800) T_a (K)	6.96	1.25	1.18
5 (800-1000) T_a(K)	8.23	1.84	1.64
Ts (K)	10.59	0.62	0.49
TPW(cm)	0.85	0.49	0.34
Mw ε	0.060	0.024	0.020
Lw ε	0.027	0.012	0.009

[a] T_a, atmospheric layer mean temperature; Ts, surface temperature; TPW, total precipitable water vapor; Mw ε , surface emissivity in the midwave region; Lw ε , surface emissivity in the longwave region.

Table 3.2. Retrieval rms of the independent dataset simulated for daytime/nighttime 418 cases, with no noise added

Layer (hPa)[a]	Dep. mean profile	Regression rtvl.	Physical rtvl.
Daytime			
1 (50-200) T_a(K)	4.46	0.90	0.84
2 (200-400) T_a(K)	3.32	1.40	1.35
3 (400-600) T_a(K)	5.62	1.13	1.07
4 (600-800) T_a(K)	6.96	1.19	1.12
5 (800-1000) T_a(K)	8.23	1.72	1.63
Ts(K)	10.59	0.41	0.23
TPW(cm)	0.85	0.34	0.27
Nighttime			
1 (50-200) T_a(K)	4.46	0.90	0.84
2 (200-400) T_a(K)	3.32	1.40	1.35
3 (400-600) T_a(K)	5.62	1.13	1.04
4 (600-800) T_a(K)	6.96	1.19	1.14
5 (800-1000) T_a(K)	8.23	1.72	1.61
Ts(K)	10.59	0.41	0.17
TPW(cm)	0.70	0.27	0.23
Emissivities			
Mw ε	0.060	0.011	0.003
Lw ε	0.027	0.007	0.005

[a] T_a, atmospheric layer mean temperature; Ts, surface temperature; TPW, total precipitable water vapor; Mw ε, surface emissivity in the midwave region; Lw ε, surface emissivity in the longwave region.

Table 4. Retrieval rms of the independent dataset simulated for daytime/nighttime 440 cases, versus daytime or nighttime dataset alone

(1)	(2)	(3)	(4)	(5)	(6)	(7)
Layer (hPa)[a]	Regression rtvl. (day/night)	Physical rtvl. (day/night)	Regression rtvl. (day alone)	Physical rtvl. (day alone)	Regression rtvl. (night[b] alone)	Physical rtvl. night[b] alone)
1 (50-200) T_a (K)	0.88	0.84	1.04	0.95	1.00	0.87
2 (200-400) T_a (K)	1.99	1.78	2.12	1.99	2.06	1.86
3 (400-600) T_a (K)	1.96	1.55	2.26	1.66	2.07	1.68
4 (600-800) T_a (K)	1.88	1.41	2.24	1.55	1.93	1.52
5 (800-1000) T_a (K)	2.66	2.43	2.98	2.75	3.07	2.84
Ts(K)	0.76	0.49	0.92	0.68	1.10	1.01
TPW(cm)	0.36	0.25	0.40	0.30	0.38	0.30
ε_{30}	0.022	0.011	0.022	0.013	0.043	0.045
ε_{31}	0.025	0.010	0.023	0.012	0.050	0.051
ε_{32}	0.024	0.009	0.023	0.011	0.050	0.048
ε_{33}	0.025	0.008	0.024	0.010	0.051	0.049
ε_{34}	0.027	0.009	0.025	0.010	0.051	0.051
ε_{42}	0.016	0.013	0.017	0.016	0.022	0.021
ε_{44}	0.012	0.008	0.013	0.010	0.018	0.016
ε_{45}	0.011	0.008	0.013	0.011	0.016	0.016
ε_{46}	0.010	0.008	0.011	0.009	0.013	0.013

[a] Ta, Atmospheric layer mean temperature; Ts, surface temperature; TPW, total precipitable water vapor; $\varepsilon_{30,\ldots,}\varepsilon_{46}$, surface emissivities.

[b] Daytime dataset but removal of surface-reflected solar beam contribution within the midwave region.

Table 5. Retrieval rms of the independent dataset simulated for daytime/nighttime 440 cases, with guess SBF, no noise added and unvaried night emissivities versus true SBF, noise added and varied night emissivities

(1)	(2)	(3)	(4)	(5)	(6)	(7)
Layer (hPa)[a]	Dependent mean profiles	Regression rtvl.	Physical rtvl. (guess SBF, no noise added, unvaried emis.)	Physical rtvl. (true SBF, no noise added, unvaried emis.)	Physical rtvl. (guess SBF, noise added, unvaried emis.)	Physical rtvl. (guess, SBF, no noise added, varied emis.)
Daytime						
1 (50-200) T_a (K)	8.11	0.88	0.84	0.85	0.87	0.87
2 (200-400) T_a(K)	6.05	1.99	1.78	1.78	1.80	1.78
3 (400-600) T_a(K)	10.92	1.96	1.55	1.56	1.60	1.58
4 (600-800) T_a(K)	12.10	1.88	1.41	1.40	1.41	1.47
5 (800-1000) T_a	13.89	2.66	2.43	2.43	2.45	2.45
Ts (K)	18.80	0.76	0.49	0.49	0.52	0.55
TPW (cm)	1.04	0.36	0.25	0.26	0.27	0.25
Nighttime						
1 (50-200) T_a(K)	8.11	0.88	0.82	0.82	0.89	0.99
2 (200-400) T_a(K)	6.05	1.99	1.75	1.75	1.80	1.76
3 (400-600) T_a(K)	10.92	1.96	1.51	1.51	1.54	1.54
4 (600-800) T_a(K)	12.09	1.86	1.33	1.33	1.37	1.46
5 (800-1000) T_a	13.90	2.66	2.40	2.40	2.44	2.46
Ts (K)	18.03	0.73	0.41	0.41	0.45	0.48
TWP (cm)	0.96	0.31	0.23	0.23	0.24	0.25
Emissivities						
ε_{30}	0.059	0.022	0.011	0.011	0.012	0.011
ε_{31}	0.064	0.025	0.010	0.009	0.011	0.011
ε_{32}	0.062	0.024	0.009	0.007	0.009	0.009
ε_{33}	0.062	0.025	0.008	0.007	0.009	0.009
ε_{34}	0.060	0.027	0.009	0.008	0.009	0.009
ε_{42}	0.043	0.016	0.013	0.010	0.012	0.015
ε_{44}	0.026	0.012	0.008	0.008	0.010	0.010
ε_{45}	0.022	0.011	0.008	0.008	0.009	0.010
ε_{46}	0.016	0.010	0.008	0.008	0.008	0.009

[a] T_a , atmospheric layer mean temperature; SBF, solar BDRF factor; Ts, surface temperature; TPW, total precipitable water vapor; $\varepsilon_{30,\ldots,}\varepsilon_{46}$, surface emissivities.

Table 6. MAS band brightness temperatures in window regions at two sounding pixels, one over Lake Mendota, and another over nearby land (20:15 UTC, 18 March, 1999)

Band	30	31	32	45	46
Lake	275.96	274.59	271.75	275.42	275.02
Land	290.23	286.25	280.04	282.56	282.78

Table 7.1. Lab measured and retrieved surface emissivities in window regions for tap water

Band	31	32	45	46
Wavelength (μm)	3.92	4.07	10.95	11.94
Measured surf. emissivity[a]	0.976	0.977	0.990	0.984
Retrieved surf. emissivity	0.975	0.980	0.992	0.985

Table 7.2. Lab measured and retrieved surface emissivities in window regions for ice

Band	31	32	45	46
Wavelength (μm)	3.92	4.07	10.95	11.94
Measured surf. emissivity[a]	0.974	0.976	0.978	0.955
Retrieved surf. emissivity	0.980	0.980	0.980	0.960

[a] Band-averaged surface emissivity at viewing angle 10 degree from nadir, weighted by the band spectral response function.

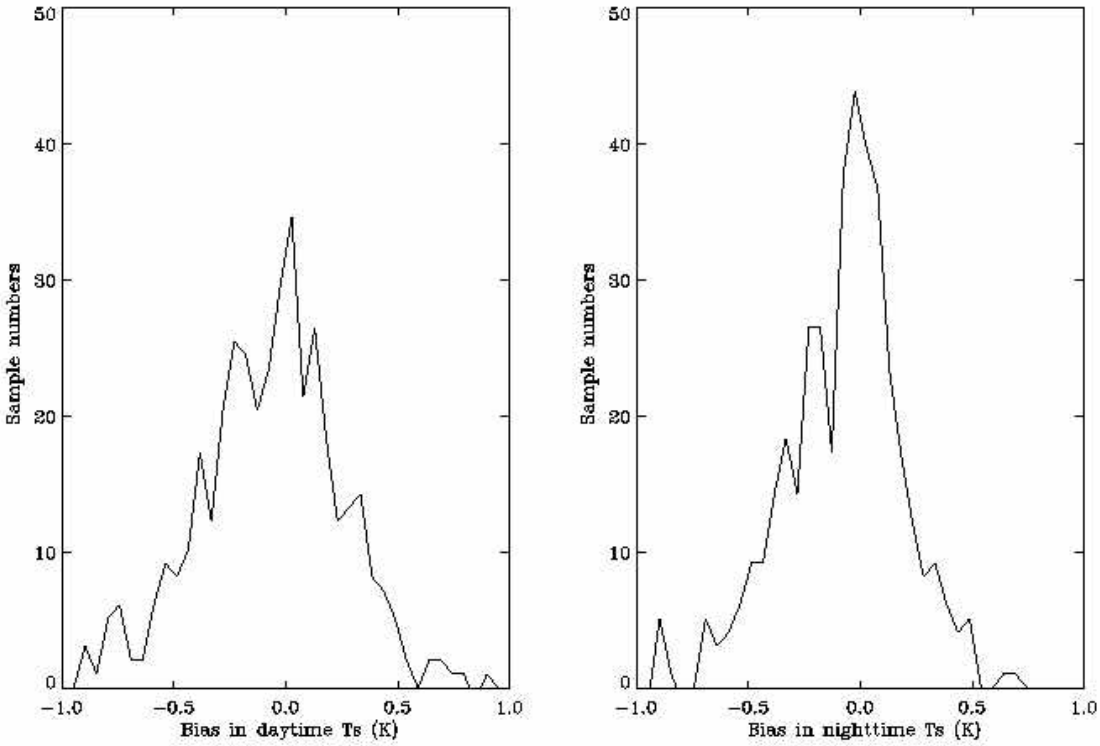
Sample numbers
Bias in daytime Ts (K)
Sample numbers
Bias in nighttime Ts (K)

(Fig. 1)

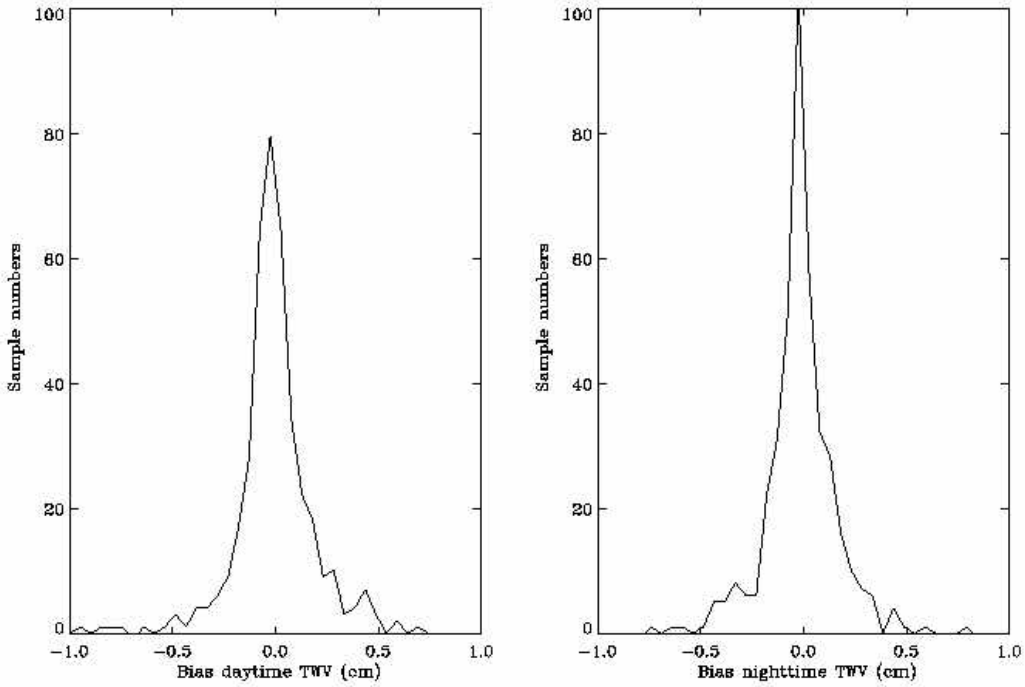
Sample numbers
Bias daytime TWV (cm)
Sample numbers
Bias nighttime TWV (cm)

(Fig. 2)

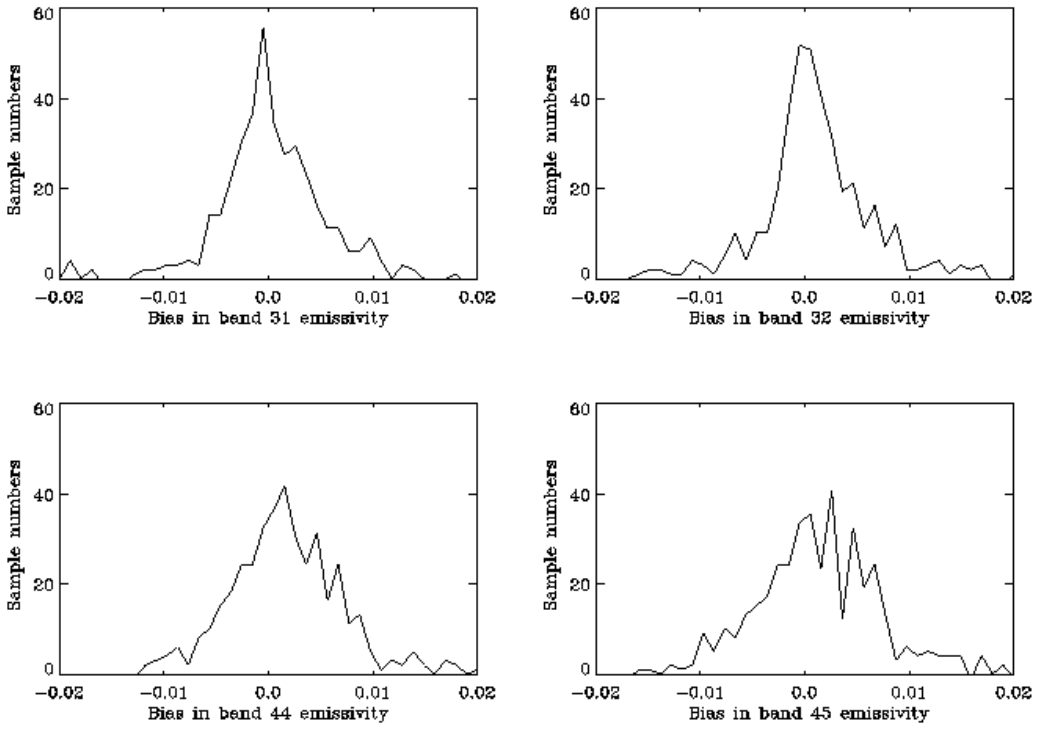
Sample numbers
Bias in band 31 emissivity
Sample numbers
Bias in band 32 emissivity
Sample numbers
Bias in band 44 emissivity
Sample numbers
Bias in band 45 emissivity

(Fig. 3)

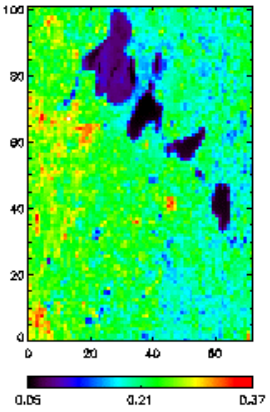

(Fig. 4)

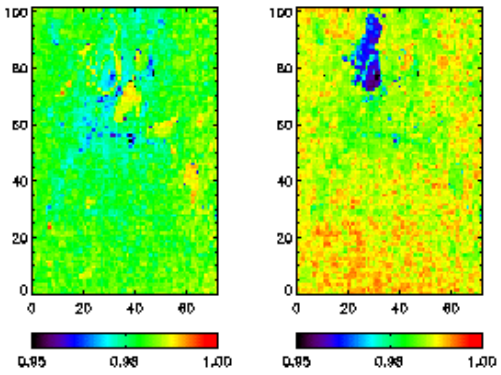

(Fig. 5)

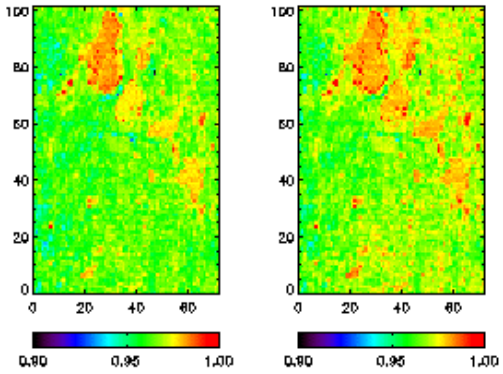

(Fig. 6)

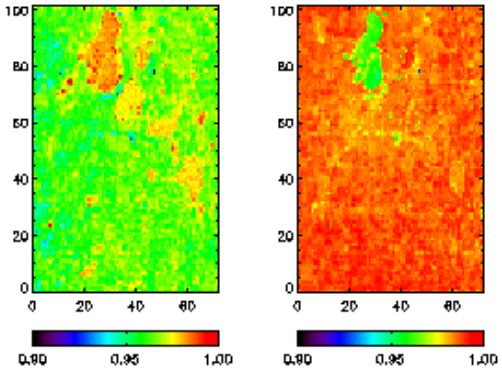

(Fig. 7)

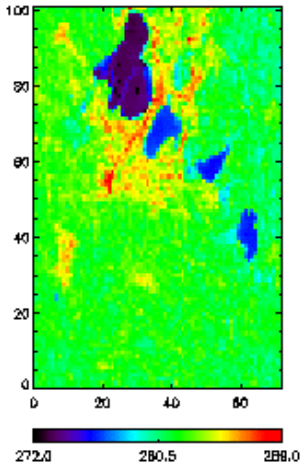

(Fig. 8)

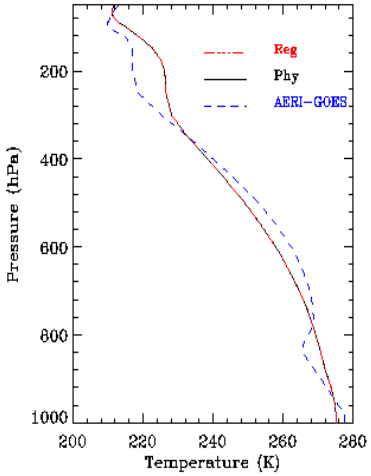

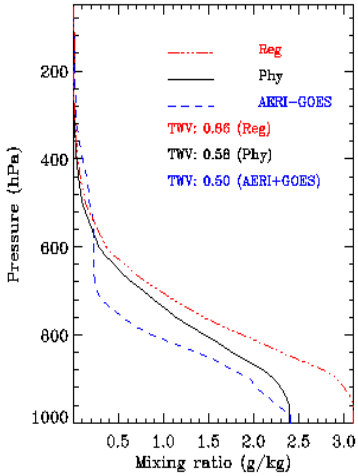

(Fig. 9)

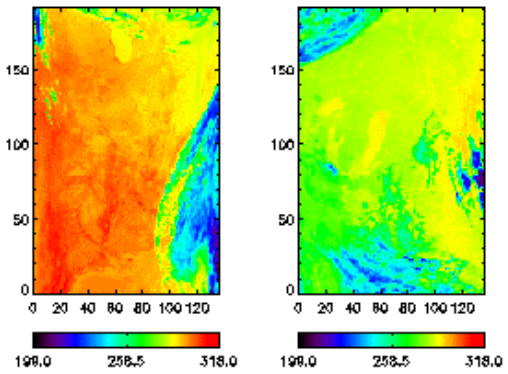

(Fig. 10)

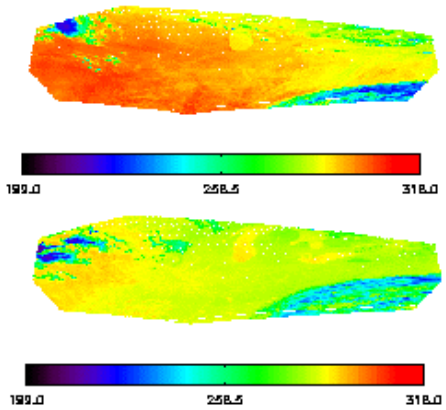

(Fig. 11)

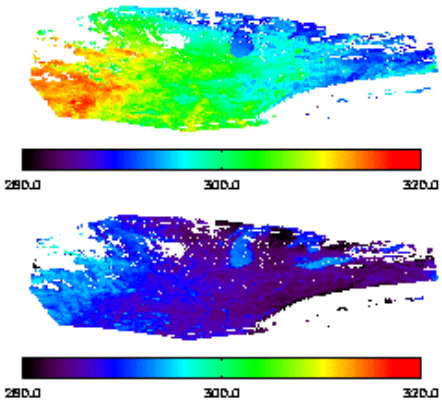

(Fig. 12)

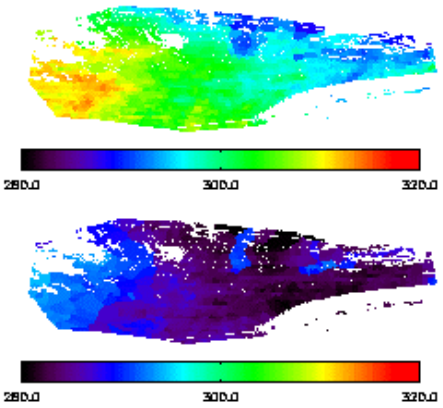

(Fig. 13)

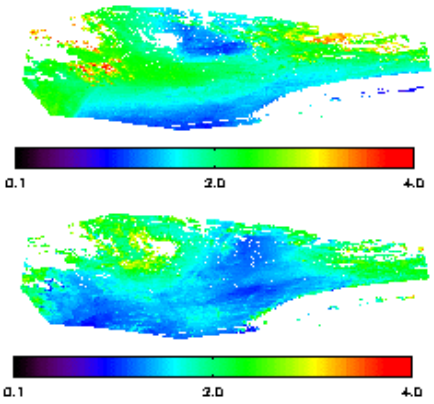

(Fig. 14)

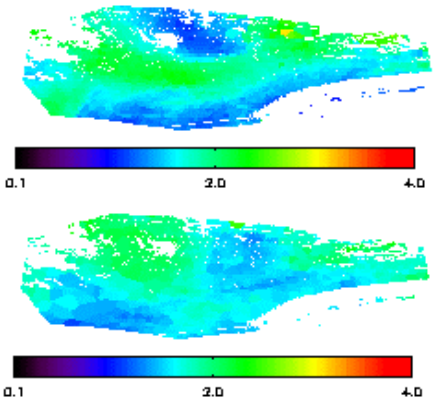

(Fig. 15)